Peng *et al.*
Journal of Engineering and Applied Science (2024) 71:198
https://doi.org/10.1186/s44147-024-00535-2

Journal of Engineering and Applied Science

RESEARCH Open Access

Bearing fault diagnosis based on enhanced Canberra distance feature in SDP image

Jigang Peng[1], Wei Wang[2] and Yongjian Sun[2*]

*Correspondence:
sunyongjian2006@163.com

[1] CEPREI Laboratory, Shandong Institute of Information Technology Industry Development, Jinan, Shandong, China
[2] School of Electrical Engineering, University of Jinan, Jinan, Shandong, China

Abstract

Feature enhancement is important in mechanical equipment fault diagnosis. A limited set of characteristic parameters is insufficient for diagnosing bearing signals with multiple fault types. The presence of noise increases the difficulty of extracting fault features from images. To address the challenge of diagnosing rolling bearing faults in complex environments, this study presents an enhanced weighted image fusion framework aimed at enhancing fault features within the images, which enables accurate diagnosis of bearing faults using a limited number of features. The proposed method encompasses four distinct stages. In the first stage, a symmetrized dot pattern method is employed to transform one-dimensional time-series data into two-dimensional images, visualizing the signal in a 2D format. In the second stage, image binarization and an improved weighted fusion method are utilized to simplify subsequent processing and enhance the image features. The third stage involves extracting the image's contrast and maximum singular value to improve the Canberra distance calculation. Finally, the enhanced Canberra distance is used for classifying bearing faults. Performance testing of the image feature enhancement is conducted on various datasets containing rolling bearings. Comparative experiments with alternative enhancement methods demonstrate the superiority of the proposed improved weighted image fusion framework. Comparative experiments with the original Canberra distance validate the effectiveness of the enhanced Canberra distance. Additionally, experiments conducted in noisy environments confirm the robustness of the proposed approach. Furthermore, the image feature enhancement method is applied to other bearing datasets, and the experimental results demonstrate its effectiveness in enhancing fault feature representation and achieving accurate diagnosis of rolling bearings.

Keywords: Rolling bearing, Symmetrized dot pattern, Variational mode decomposition, Canberra distance, Improved weighted average, Fault diagnosis

Introduction

The smooth operation of mechanical equipment is essential for ensuring efficient industrial production. The health status of mechanical equipment can be determined through diagnostic techniques. Analyzing the diagnostic results can help reduce the occurrence of faults. Analyzing the health of equipment enables planned maintenance and prevents failures from occurring in advance [1].

Fault diagnosis of mechanical equipment primarily involves analyzing the collected signals [2]. Early signal processing methods focus on time domain analysis, frequency domain analysis, and time–frequency domain analysis [3]. Time domain analysis enables direct processing of the collected time series [4]. Frequency domain analysis involves separating different frequencies of signals and analyzing the frequency components of interest in detail. It is particularly suitable for processing nonstationary signals [5]. For instance, the empirical wavelet transform (EWT) based on the Fourier transform can be employed to construct adaptive wavelets. This decomposition method is suitable for analyzing nonstationary signals and allows for the adaptive decomposition of signals [6]. In [7], empirical mode decomposition (EMD) and its improved versions are discussed. The use of signal decomposition methods enables better processing and analysis of signals. In fault diagnosis, it is possible to directly extract features from signals. Differentiation of various data sets is achieved through the differences in these features [8]. Additionally, image-formatted data is better suited for novel intelligent methods [9]. For instance, machine learning and deep learning have found broad application in signal analysis [10]. In [11], 96 features were extracted from color fundus images. Accurate diagnosis of diabetic retinopathy is achieved through the established artificial intelligence classification model. This reference provides an artificial intelligence model with low computational complexity and high classification accuracy. The model effectively addresses nonlinear dynamical problems.

Various techniques can be employed to enhance images, such as histogram equalization, contrast enhancement, texture enhancement, and image filtering. It is important to adopt appropriate processing methods for different types of images. Image enhancement in mechanical fault diagnosis aims to emphasize fault features while suppressing irrelevant ones. Bai et al. [12] utilized the channel selection method to enhance performance for extracting the features of interest in the image. On one hand, this method can decrease computation requirements and mitigate the impact of noise [13]. Kim et al. [14] used a multi-scale convolution filter to enhance fault features. This processing method facilitates the diagnosis of gearbox faults. Wu et al. [15] applied an adaptive logarithmic normalization method to enhance the quality. This method enhances image details and yields favorable results in rolling bearing tests. Jablonski et al. [16] aimed to obtain a clearer spectrum image, thus employing STFT for automatic analysis of image conversion parameters. This method can make the spectrum image more clear. Enhancing image definition can result in more prominent feature components of the signal. Wodecki et al. [17] employed a nonnegative matrix decomposition method to differentiate between the image's features and noise. This image enhancement method can mitigate the impact of noise. It enables the filtration of specific noise components for fault diagnosis in rotating machinery. Reinhold et al. [18] applied the redistribution method to process the energy distribution of the image's time–frequency spectrum. This image enhancement method enhances the spectrum's robustness against noise. Therefore, image enhancement methods play a significant role in using images to diagnose mechanical equipment.

There are several widely used methods for signal transformation of image in the fault diagnosis of mechanical equipment, including recursive images, scalogram, fast kurtogram, Gramian angular field, and Markov transition field. Consequently, image enhancement

methods play a significant role. Enhanced images can better highlight signal characteristics, thus providing an improved basis for fault classification. Peng et al. [19] developed an adaptive image segmentation algorithm that effectively mitigates distortion in two-dimensional images obtained from scanning imaging. Long et al. [20] employed the scale invariant feature transform to extract features from the symmetrized dot pattern. Wang et al. [21] converted signals into images using short-time Fourier transform (STFT). They then used a convolutional neural network for fault classification. Tang et al. [22] employed the Gramian angular summary field to convert rotational signals into diagnostic images. This method exhibits excellent performance in processing noisy signals. Li et al. [23] utilized a weighted horizontal visibility map to convert signals into images, specifically focusing on image edge processing. The advantage of this image enhancement method lies in its ability to attenuate the influence of noise. Fang et al. [24] employed a data conversion image method for fault diagnosis. Additionally, they proposed a spatial attention mechanism for adjusting image outputs. This image enhancement method exhibits robust anti-interference capabilities. Wang et al. [25] introduced a temporal-spatial graph method for converting signals to images. They utilized the graph-mapped spectrum for diagnosing bearing faults. This method enhances the frequency features of the signal and is applicable for diagnosing bearing faults. In conclusion, image processing methods are extensively employed for fault diagnosis of mechanical equipment [26]. Therefore, image processing and enhancement methods are also a very important research direction.

The vibration signal of rolling bearings is a nonstationary signal. Traditional time-domain and frequency-domain analysis methods cannot intelligently extract fault features. Image-based fault diagnosis methods can achieve intelligent fault diagnosis. However, the symmetrized dot pattern method, which converts one-dimensional signals into two-dimensional images, increases data dimensionality. Images contain a lot of redundant information, so enhancing fault features in the image can improve the effectiveness of fault diagnosis. In practical industrial production, signals are often influenced by noise. Studying the enhancement of fault features through image denoising is meaningful. It improves fault classification effectiveness. Therefore, the purpose of this paper is to achieve accurate fault classification through feature enhancement of images.

In this paper, a new method of image enhancement is proposed to process the synchronized dot pattern after signal conversion. The method of image enhancement is used to diagnose the fault on the bearing test bed. The method of image enhancement is also verified under different noise signals. The rest of this paper is arranged as follows. In the "Methods/experimental" section, methods for image enhancement are introduced. In the "Methods" section, relevant experiments were designed, and the experimental results were analyzed. In the "Results and discussion" section, comparative experiments were designed to verify the effectiveness of this method. In the "Limitations and implications of research findings in the current research context" section, the potential challenges of SDP images are discussed. The conclusion is given in the "Conclusion" section.

Methods/experimental

Aim

This study aims to classify various types of bearing faults using the vibration signals of rolling bearings, employing techniques such as image conversion and image

enhancement. Specifically, the research focuses on addressing the classification problem of bearing fault types under noisy conditions.

Design and setting

This paper presents the development of the SDP image feature enhancement method and the enhancement of Canberra features for fault detection. As illustrated in Fig. 1, the method is primarily divided into two parts: image enhancement and feature extraction. The improved grayscale-weighted average method and the utilization of maximum singular value and contrast play vital roles in enhancing the Canberra distance.

The research methodology in this paper is divided into three parts. The specific process is described as follows: In the first part, a method for image feature enhancement is proposed. In the second part, an improved method for extracting Canberra distance features is presented. In the third part, a workflow for fault diagnosis of rolling bearings is proposed. The diagnostic effectiveness of this method is validated through experiments.

In the image enhancement phase, data from each working condition is selected separately. Random selection of data with a length of 6000 is performed. The selected data is divided into 10 groups. Each group has an average of 600 data points. The 10 groups of data are first converted into SDP images. These SDP images are then transformed into grayscale images. Then, an enhanced image is obtained using the improved grayscale-weighted averaging method. The purpose of this process is to highlight fault features.

In the feature extraction part, the first step is to calculate the maximum singular value and contrast of the enhanced image. Then, the Canberra distance between the 10 grayscale images and the enhanced image is calculated. Use the three obtained features to

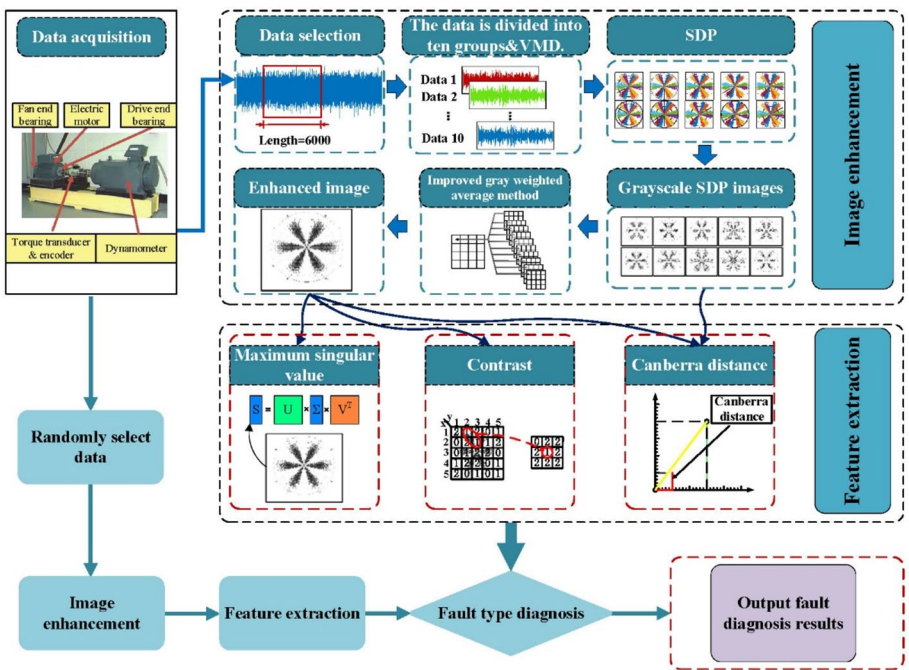

Fig. 1 Design of the flowchart for the proposed method

obtain improved Canberra distance features. Finally, utilize these features to achieve fault classification for rolling bearings.

In the experiment, the fault types and data are first randomly selected. Then, the data undergoes the same image enhancement and feature extraction processes. By comparing the obtained features with the known working condition features, the diagnosis of bearing fault types is achieved.

Participants or materials

The rolling bearing dataset used in this study comes from the bearing data center at Case Western Reserve University (CWRU). The experimental device is depicted in Fig. 2. The device is capable of inducing bearing faults under varying loads and fault diameters. Its primary working conditions involve inner ring, outer ring, and ball faults. The dataset is further divided into single-point defects of varying sizes. At different sampling frequencies, the original time-domain vibration signal is formed.

This data set collects time-series data of drive end, fan end, and base. The time series of the driving end is used in this experiment. The specifications of the bearing used are shown in Table 1. All the data are at 12-kHz sampling frequency. The total length of each data is 120,000. Each group of data is divided into two parts. The data length of each part is 60,000. One part of the data is used for feature extraction. The other part of the data is used for experimental validation.

Processes and methodologies

This study utilizes variational mode decomposition and an enhanced weighted average method to enhance the fault features in symmetrized dot pattern (SDP). The diagnostic accuracy is considered as the evaluation metric. This method is employed to achieve accurate classification of rolling bearing faults in a noisy environment and to exploit the fault data in the images. To achieve effective diagnosis, four processing methods are employed: variational mode decomposition (VMD), symmetrized dot pattern, an

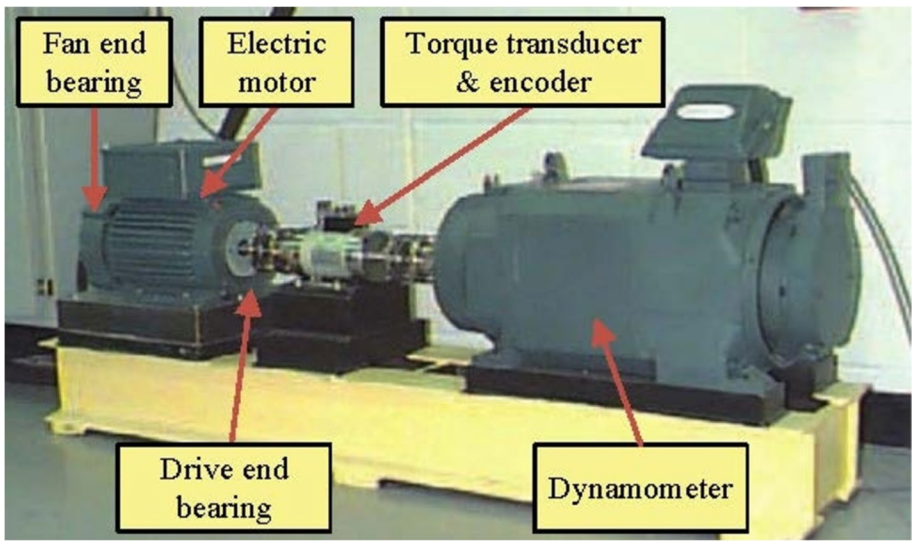

Fig. 2 Experimental platform

Table 1 Types of rolling bearings

Fault type	Load (HP)	Fault diameter (mm)
Normal status	1	-
Inner ring fault 1	0	0.1778
Inner ring fault 2	2	0.1778
Inner ring fault 3	3	0.5334
Outer ring fault 1	1	0.3556
Outer ring fault 2	1	0.5334
Outer ring fault 3	1	0.1778
Ball fault 1	1	0.1778
Ball fault 2	2	0.1778
Ball fault 3	2	0.5334

improved weighted average method, and improved Canberra distance feature. Firstly, the signal is denoised using variational mode decomposition. Then, the denoised signal is transformed into an image using the SDP method. The enhanced weighted average method is utilized to enhance the fault features in the image for fault data mining. Finally, the improved Canberra distance feature is used to extract image features for fault diagnosis.

Ethics approval and consent

This study does not involve human participants, data, or tissue, nor does it involve animals. Therefore, ethics approval and consent are not applicable.

Statistical analysis

Statistical analysis was not conducted in this study. Ethics approval and consent are not applicable, and statistical analysis is not performed.

Methods

Variational mode decomposition

Variational mode decomposition can adaptively decompose the original signal, which can be transformed into the corresponding variational problem construction and solution [27]. It is mainly divided into the following three steps. In Hilbert transform to find the analytical signal, by multiplying with $e^{-j\omega_k t}$, the formula is as follows:

$$(\delta(t) + \frac{j}{\pi t}) * v_k(t) \tag{1}$$

where.

$\delta(t) =$ Dirac function.

$\gamma(t) =$ The distribution function.

$v_k(t) =$ The kth mode component.

The analysis signal of $v_k(t)$ is calculated by Hilbert transformation [28]. By multiplying with the operator $e^{-j\omega_k t}$, the central band of $v_k(t)$ is modulated to the corresponding

baseband, as shown in Eq. 2. Estimate the bandwidth of the signal, that is, calculate the square norm L2 of the demodulation gradient, as in Eq. 3.

$$[(\delta(t)+\frac{j}{\pi t})*v_k(t)]e^{-j\omega_k t} \tag{2}$$

$$\begin{cases} \min\limits_{\{v_k\}\{w_k\}} \{\sum_k ||\partial_t[(\delta(t)+\frac{j}{\pi t})*v_k(t)]e^{-j\omega_k t}||^2\} \\ s.t. \sum_k v_k = s \end{cases} \tag{3}$$

where.

$\omega_k =$ The center frequency of each component signal.

$* =$ Convolution operation.

$f =$ The input signal.

The VMD method adaptively decomposes the signal by searching for the optimal solution of the aforementioned constrained variational model. During the iterative solving process, the central frequency and bandwidth of each component are gradually updated, and ultimately, the IMF components are adaptively partitioned based on the signal's own frequency domain characteristics. When solving this model, it is necessary to introduce the quadratic penalty factor α and the Lagrange operator $\lambda(t)$. This transformation transforms the above constrained variational problem into the following unconstrained variational problem:

$$\begin{gathered} L(\{v_k\},\{\omega_k\},\lambda) = \\ \langle\lambda(t), f(t)-\sum_k v_k(t)\rangle + \| f(t)-\sum_k v_k(t) \|_2^2 + \alpha \sum_k \| \partial_t(\sigma(t)+\frac{j}{\pi t})v_k(t)e^{-j\omega_k t}) \|_2^2 \end{gathered} \tag{4}$$

where.

$\sum_k v_k(t) =$ The sum of IMF components.

$\alpha =$ Quadratic penalty factor.

$\lambda(t) =$ Lagrange operator.

By alternately updating $v_k(t)$, ω_k, and λ, the aim is to find the saddle point in the expression. The updating process of each modal component is as follows:

$$v_k^{n+1} = \arg\min_{v_k\in X}\{\| f(t)-\sum_i v_i(t)(t+\frac{\lambda(t)}{2}) \|_2^2 + \alpha \| \partial_t[(\delta(t)+\frac{j}{\pi t})v_k(t)]e^{-j\omega_k t} \|_2^2\} \tag{5}$$

Convert the above equation into a frequency domain expression as follows:

$$\hat{v}_k^{n+1} = \arg\min_{\hat{v}_k, v_k\in X}\{\| \hat{f}(t)-\sum_i \hat{v}_i(\omega)+\frac{\hat{\lambda}(\omega)}{2} \|_2^2 + \alpha \| j\omega[(1+sgn(\omega+\omega_k))\hat{v}_k(\omega+\omega_k)] \|_2^2\} \tag{6}$$

By solving the equation, the optimal solution to the optimization problem can be obtained as follows:

$$\hat{v}_k^{n+1}(\omega) = \frac{\hat{x}(\omega)-\sum_{i=1,i\neq k}^{K}\hat{v}_i(\omega)+\frac{\hat{\lambda}(\omega)}{2}}{1+2\alpha(\omega-\omega_k)^2} \tag{7}$$

where

$K =$ the number of decomposition layers.

Principle of symmetrized dot pattern

Symmetrized dot pattern (SDP) is a simple image conversion method. It maintains the relationship between amplitude and frequency of the signal [29]. For discrete signals, this transformation can obtain corresponding points at different positions in polar coordinates. For the sampled discrete signal, this conversion can obtain corresponding points at different positions of polar coordinates. The distribution of points can directly display the features of signals. The schematic diagram of SDP conversion is shown in the Fig. 3.

For a time series, x_i represents the i-th sampling point of the signal, and $x_{(i+l)}$ is the sampling point after adjacent time l. According to the SDP conversion principle, sampling points at different times can be converted to polar coordinate space $P(r(i), \theta(i), \phi(i))$. The radius from the center point can be expressed as follows:

$$r(i) = \frac{x_i - x_{mean}}{x_{max} - x_{min}} \tag{8}$$

where

$x_i =$ The i-th signal value

$x_{min} =$ The minimum value in the signal sequence.

$x_{max} =$ The maximum value in the signal sequence.

$x_{mean} =$ The mean value of the signal sequence.

The anticlockwise rotation angle $\theta(i)$ and the clockwise rotation angle $\phi(i)$ along the initial line are projected by the adjacent points $x_{(i+l)}$. The rotation angle can be expressed as follows:

$$\theta(i) = \varphi + \frac{x_{i+l} - x_{mean}}{x_{max} - x_{min}} \zeta \tag{9}$$

$$\phi(i) = \varphi - \frac{x_{i+l} - x_{mean}}{x_{max} - x_{min}} \zeta \tag{10}$$

where.

$\zeta =$ The angular gain factor of the plot.

$\theta(i) =$ The angle of counterclockwise rotation along the initial line.

$\phi(i) =$ The angle of clockwise rotation along the implementation line

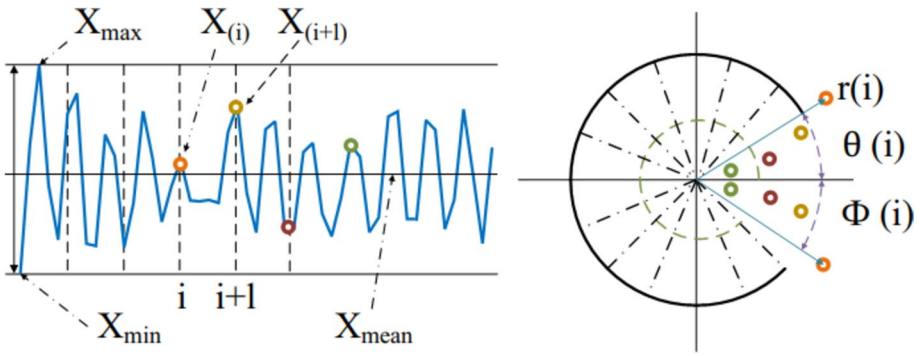

Fig. 3 Schematic diagram of symmetrized dot pattern

φ = The symmetrical rotation angle of the mirror. $\varphi = 360 \times m/n, (m = 1,2,\ldots,n)$

l = The time interval, usually between 1 and 10.

In this paper, SDP provides a way to convert data into images. This method converts one-dimensional time series into two-dimensional space. The features of the time series are converted into features such as contrast, texture, and shape in the image. This provides a suitable data format for subsequent feature enhancement. Compared with time–frequency analysis and raw signal-based methods, the proposed method has better adaptability to nonstationary signals. The data features are integrated into the features of the image. Image data is more convenient for intelligent extraction and analysis.

Image feature enhancement

The grayscale image is composed of different grayscale values. The value of each pixel is in the range of 0 to 255 [30]. Image graying is mainly to convert color images into grayscale images. The conversion formula is shown in Eq. 7. The grayscale image converts the three-channel color image into a grayscale matrix.

$$Gray(i,j) = a \times R(i,j) + b \times G(i,j) + c \times B(i,j) \tag{11}$$

where.

$R(i,j)$ = The red channel pixel value.

$G(i,j)$ = The green channel pixel value.

$B(i,j)$ = The blue channel pixel value.

a, b, and c = The weights of pixel values of different channels.

$Gray(i,j)$ = The grayscale values of the i th row and j th column of the grayscale image.

Image fusion is a process that involves processing and synthesizing images. Images are collected from multiple channels to create high-quality images. The purpose of image fusion is to weaken the uninterested content in the image. It also aims to suppress noise and highlight the key information of the image. Image fusion methods are mostly used to process remote-sensing images, infrared images, and medical images. Pixel level fusion is the process of finding the mean of the corresponding pixels in different images. The calculation formula can be expressed as follows:

$$FuImage(i,j) = (\sum_{i=1}^{N} I_i(i,j))/N \tag{12}$$

where.

$I_n(x,y)$ = The i th input grayscale image.

N = The number of images.

$G(x,y)$ = The fused pixel matrix.

The equation combines multiple images $I(i,j)$ into one image $FuImage(i,j)$. The pixel values of $FuImage(i,j)$ are determined by the average pixel values of all images.

This simple grayscale averaging method cannot handle images well. For grayscale SDP images, this paper proposes an improved grayscale-weighted average method.

Different from the original method, this method first performs statistics on the gray values of the input images. The number of pixels that meet the condition is denoted as N_{px}. The pixel values of the enhanced image are determined based on the comparison between N_{px} and the threshold T. When N_{px} is less than the threshold, the pixel value of the enhanced image is determined by the input image. When N_{px} is greater than the threshold, the pixel value is set to 255. The specific mathematical formula is as follows:

$$EnhanceImage(i,j) = \begin{cases} \frac{(\sum_{i=1}^{N} \omega_n \times I_n(i,j))}{(N-N_{px})} & N_{px} < T \\ 255 & N_{px} \geq T \end{cases} \tag{13}$$

where.

N_{px} = The number of pixels with a value of 255 corresponding to multiple images

T = The threshold range between 0 and N

ω = The weight value

$EnhanceImage(i,j)$ = The grayscale values of the i th row and j th column of the enhanced image.

Original canberra distance

The distance reflects the similarity between two samples. Manhattan distance calculates the sum of longitudinal and transverse distances. The Canberra distance is normalized based on the Manhattan distance. This processing eliminates the dimensional influence between different distances.

For two n-dimensional vectors, calculate the distance between the corresponding elements separately. Finally, summing n distance values can obtain the distance between two vectors. The Canberra distance between two vectors is expressed as follows:

$$d(p,q) = \sum_{m=1}^{n} \left| \frac{p_m - q_m}{|p_m| + |q_m|} \right| \tag{14}$$

where.

p and q = Respectively vectors of the same length.

$d(p,q)$ = The Canberra distance between vector p and vector q

For two $n \times n$ matrices, first calculate the distance between the corresponding row vector. Then average the distance of n row vector to get the distance between the last two images. The Canberra distance between two matrices can be expressed as follows:

$$d_{Canberra} = \frac{\sum_{i=1}^{n} d(p_i - q_i)}{n} \tag{15}$$

where.

$d_{Canberra}$ = The average value of Canberra distance.

p_i = The i th row vector.

n = The number of rows in the matrix.

Improved canberra distance feature in SDP image

A grayscale image is a matrix. Each element of this matrix has grayscale values between 0 and 255. Each pixel in the image corresponds to a different grayscale value. Therefore,

the Canberra distance can be used to extract features between two grayscale images. However, the Canberra distance cannot fully meet the diagnosis of bearing faults. In order to improve the performance of fault diagnosis, an improved Canberra distance is proposed based on the original Canberra distance. Two parameters are mainly used for improvement. These two parameters are singular value and contrast. The improved Canberra distance is shown in Eq. 12.

$$D = (\sigma_{max}/(k \times d_m))Con \tag{16}$$

where:

σ_{max} = The maximum singular value.

Con = The contrast of an image.

D = Enhanced Canberra distance.

k = A positive integer, and its main function, is to adjust the size of features and expand differences in features.

Singular value decomposition (SVD) is used in signal processing, data fusion, data reduction, and image denoising. Its principle is to transform the original complex matrix into three basic matrices. Let the original matrix be S, and the matrix is a real matrix with rank greater than 0. Then the singular value of matrix S is decomposed into the following:

$$S = U\begin{pmatrix} \sum & 0 \\ 0 & 0 \end{pmatrix}V^H \tag{17}$$

where.

S = The real matrix of $m \times n$ order.

U is a unitary matrix of order $m \times m$

V = A unitary matrix of order $n \times n$

$V \times H$= The conjugate transposition of$V$

$\sum = \begin{pmatrix} \sigma_1 & \cdots & 0 \\ \vdots & \cdots & \vdots \\ 0 & \cdots & \sigma_{max} \end{pmatrix}$, σ_{max} represents the maximum singular value. $\sigma_1 \geq \sigma_2 \geq \sigma_3 \geq \cdots \sigma_{max} > 0$.

A grayscale image can also be extracted by singular value decomposition. The singular value of the matrix can represent the feature information in the matrix. Here, the maximum singular value is selected as the parameter to improve the Canberra distance.

The gray-level co-occurrence matrix (GLCM) describes the texture characteristics of an image by analyzing its gray space. Figure 4 is a schematic diagram of converting an image to a gray-level co-occurrence matrix. The gray-level co-occurrence matrix describes the correlation characteristics of gray levels in an image based on the relationship between gray levels of pixels. The principle of the gray-level co-occurrence matrix is to count the number of times a certain pixel appears at a specific angle.

Figure 4a is a geometric representation of the gray-level co-occurrence matrix. $F(i,j) = a$ indicates that the pixel value in the i th row and j th column of the image is a. X represents the horizontal distance from the pixel value a to the pixel value b. Y represents the vertical distance from the pixel value a to the pixel value b. Figure 4b is a pixel value matrix of the original image. The numerical value in the box represents the grayscale value of the pixel. Figure 4c is a gray-level co-occurrence matrix. The grayscale

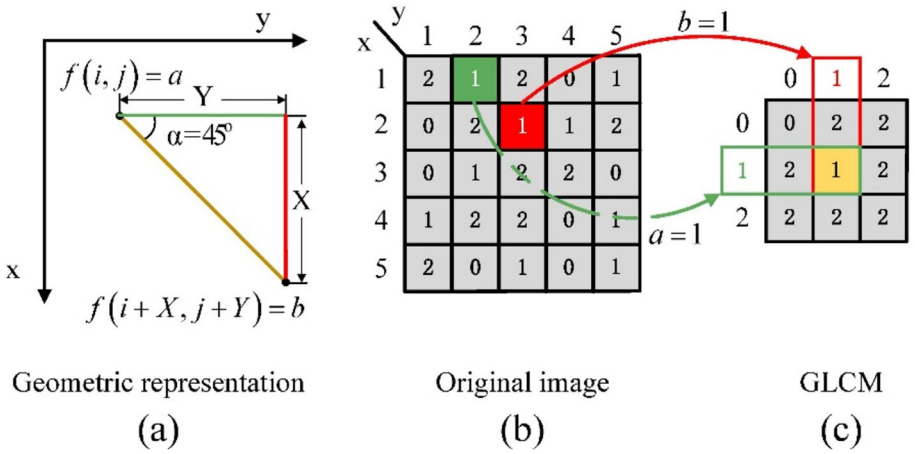

Fig. 4 Schematic diagram of gray-level co-occurrence matrix. Geometric representation (**a**). Original image (**b**). GLCM (**c**)

value of the original image ranges from 0 to 2. Therefore, the horizontal and vertical directions of the gray-level co-occurrence matrix are also within the range of 0 to 2. When $\alpha = 45°, X = 1, Y = 1$, the gray level co-occurrence matrix conversion process is shown in the figure. The number of occurrences from green pixel value 1 to red pixel value 1 is 1. Therefore, the value corresponding to the yellow position of the gray-level co-occurrence matrix is 1. Different features of an image can be extracted from the gray-level co-occurrence matrix, such as the energy, correlation, and contrast of an image. Because contrast reflects the clarity and depth of the image texture. Here, contrast is used to improve the Canberra distance. The formula for calculating contrast is shown in Eq. 14.

$$CON = \sum_i \sum_j (i-j)^2 P(i,j) \tag{18}$$

where.

$P(i,j) =$ The distribution probability of the distance (i,j) between pixel values.

Results and discussion

Based on the fault diagnosis scheme outlined in Fig. 1, this experimental study developed a program for feature enhancement and extraction. Additionally, precision experiments were designed for verification. During the image enhancement stage, the original signal is processed to enhance fault features and reduce noise interference. Variational mode decomposition (VMD) is employed to decompose the nonstationary bearing signals from each working condition. In Fig. 5, the original signals from 10 working conditions are decomposed into two components. The blue line represents the time series of the original signal. The red line represents the time series of the first intrinsic mode function (IMF1) after VMD, and the yellow line represents the time series of the second mode function (IMF2). Through the figure, we can observe that the first intrinsic mode function (IMF 1) retains the characteristic information of the original signal. Compared to the IMF 2 signal, the IMF 1 signal exhibits more pronounced features. Consequently, the first component is selected as the decomposed data.

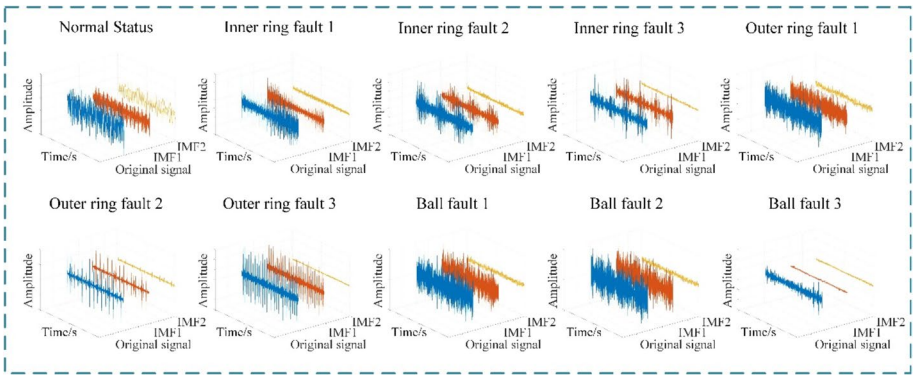

Fig. 5 Time domain images of components after VMD under different fault conditions

According to the SDP transformation method, the IMF1 signal is converted into an image format. The signals and images of different fault types are shown in Fig. 6. Due to the VMD processing, the features of the signal are more apparent. These features can be observed more intuitively through the SDP image.

The size of each SDP image is 750×750. When the signal is converted into an image, the features of the vibration signal become the shape, texture, and thickness of the image. The images of different types of signals are different. For instance, the normal working condition displays a smoother fan flap shape, while inner ring fault 3 exhibits a slenderer shape. Outer ring fault 2 appears in a discrete state, while ball fault 3 is more concentrated. However, due to nearly identical original signals for ball fault 1 and ball fault 2, the resulting converted images also bear strong resemblance. Different types of faults can be classified through the analysis of images. However, it is still difficult to extract the features of weak faults.

In order to enhance the weak fault features in the signal, this paper proposes an image feature enhancement method. Firstly, the time series decomposed by variational mode decomposition are uniformly divided into 10 groups. The SDP transformation method is used to plot the 10 groups of data for each operating condition into images. Since the color of the images does not highlight the features of the signal, it is necessary to process the images into grayscale. The grayscale images for each operating condition are shown in Fig. 7. Each row in the figure represents one operating condition, and each operating condition contains 10 images.

From Fig. 7, we can observe that there are differences in the SDP images under different operating conditions. This indicates that the SDP images can reflect the fault features of the signal. However, there are also varying degrees of differences between the images under the same operating condition. This indicates that the transformed images of the signal are not stable. Additionally, random points generated by noise in the images also affect the stability of the images. The instability of the images can lead to errors in fault diagnosis. To solve this problem and obtain stable images, we propose an improved weighted averaging method for image processing.

The schematic diagram of this improved SDP image-weighted averaging method is shown in Fig. 8. It is a pixel-level image fusion algorithm. The algorithm can be divided into four parts: pixel value acquisition, pixel value judgment, counting pixel

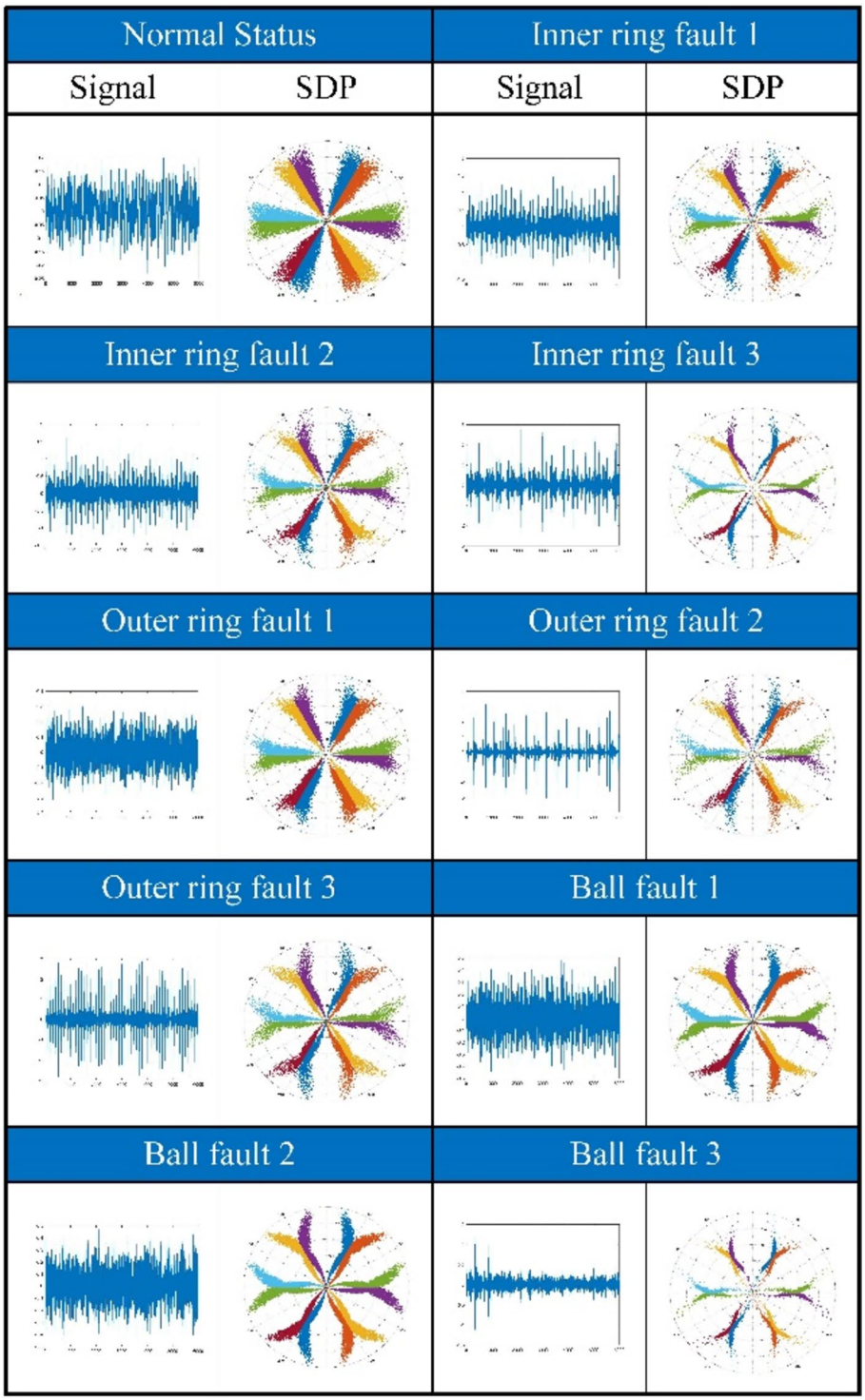

Fig. 6 Time domain image and SDP image under different working conditions

values, and pixel synthesis. The detailed explanations for these four parts are as follows:

In the pixel value acquisition stage, it is necessary to traverse the pixel values of each row and column of 10 images. In the pixel value judgment stage, the pixel values of

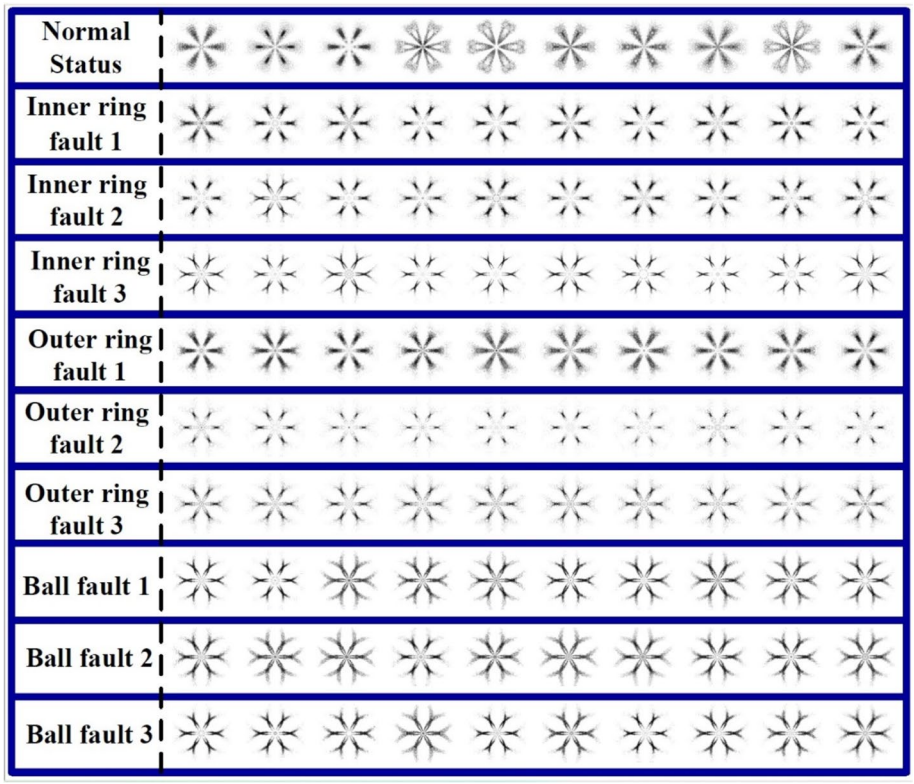

Fig. 7 Gray SDP images under different working conditions after grouping

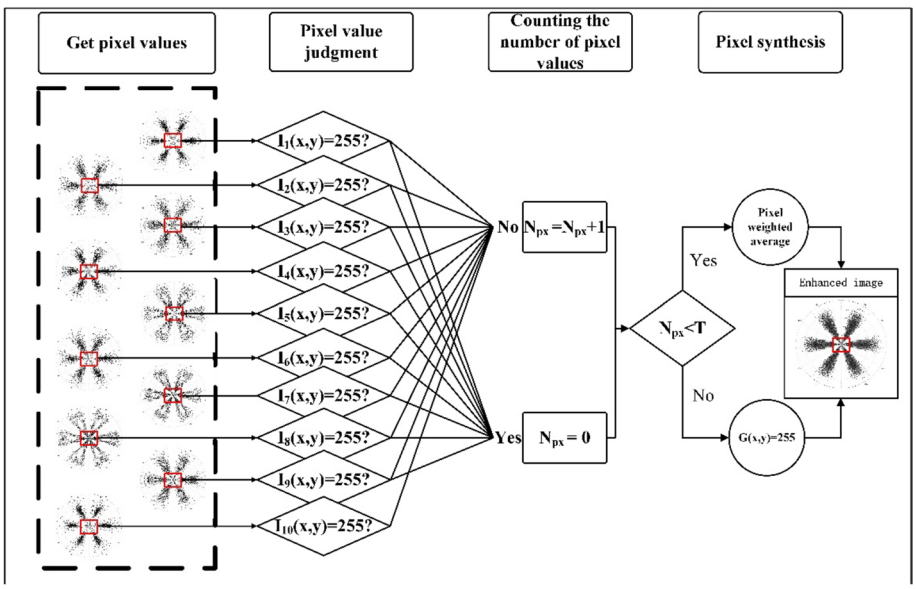

Fig. 8 Flow chart of improved grayscale-weighted average method

the same row and column of 10 images are compared. It determines whether the pixel value is equal to 255. In the counting pixel values stage, the number of times that the pixel value is not equal to 255 is counted. The count can range from 0 to 10. In the pixel

synthesis stage, the relationship between the count and the threshold value is determined. When the count is less than the threshold value, the enhanced pixel value of the image is obtained through weighted averaging. When the count is greater than or equal to the threshold value, the enhanced pixel value of the image is set to 255.

By using the above image feature enhancement method, random points in the image can be eliminated. And the fault feature information in the 10 images is preserved. The enhanced images have more obvious feature information compared to the original SDP images. In Fig. 9, SDP images under different thresholds are listed. In the figure, each column represents an enhanced image under a different threshold. By observing, it can be noticed that a larger threshold results in clearer image contours. A smaller threshold preserves less information in the image. Different operating conditions exhibit different behaviors under different thresholds. For example, the image under normal conditions is barely visible when the threshold is less than 2. This indicates that a threshold that is too small does not effectively reflect the signal features. When the threshold is set to 10, the images between different operating conditions have a high degree of similarity. This is not conducive to fault classification.

In order to determine the optimal image enhancement effect at different threshold values, we extract and analyze the features under each threshold condition. After

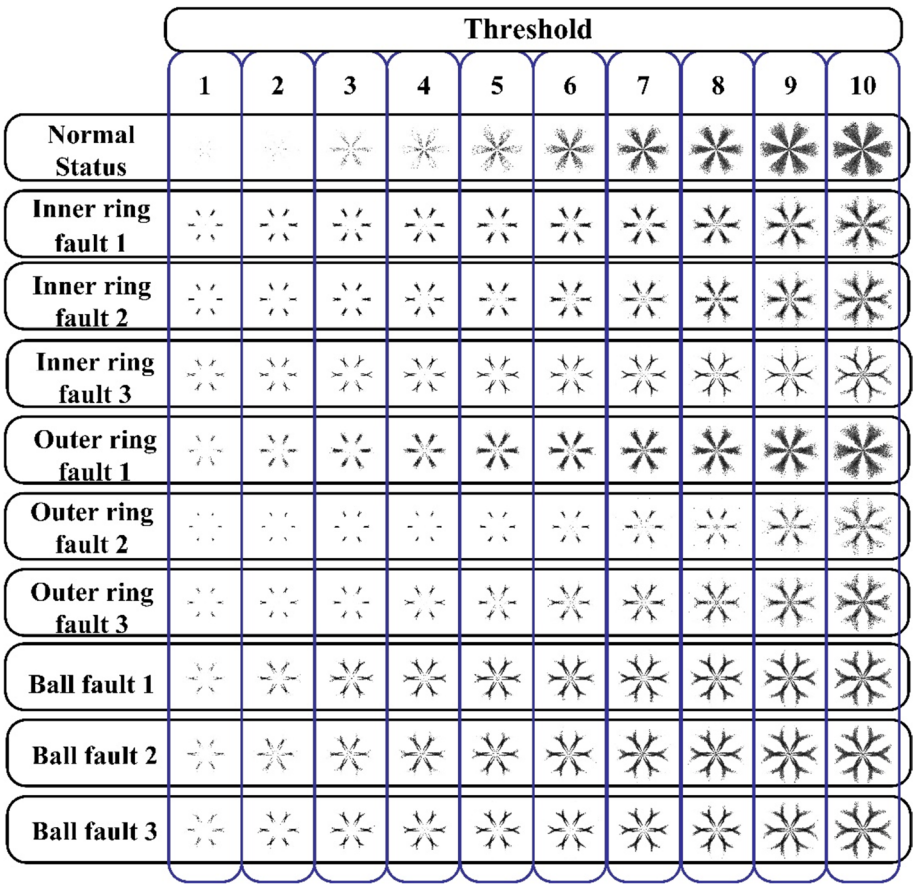

Fig. 9 Enhanced images with different thresholds under various conditions

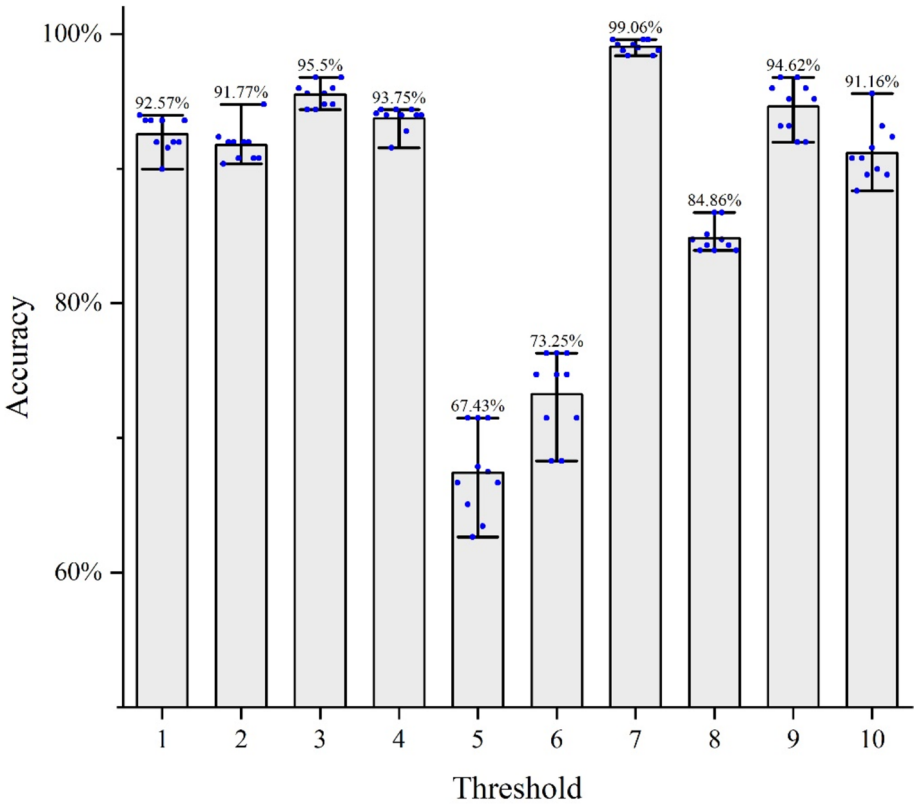

Fig. 10 Accuracy of diagnosis with different thresholds

conducting an accuracy test, the results are presented in Fig. 10. The height of the histogram represents the average accuracy under different threshold conditions. Each blue dot in the figure corresponds to an accuracy test result. The top horizontal line represents the highest accuracy achieved in the test set. The bottom horizontal line represents the lowest accuracy. The figure shows that the accuracy rate reaches its peak at a threshold value of 7. We believe that the reason for this result is that the fault characteristics are most prominent at this threshold. When the threshold is low, too much information in the image is eliminated. On the other hand, when the threshold is high, excessive noise information is retained. According to Eq. 13, the threshold T is set to 7. When the number Npx of pixels with a value of 255 in the original SDP image is between 7 and 10 (inclusive), the pixel value of the enhanced image is set to 255. When the number is less than 7, the average of the grayscale values of pixels that are not 255 is taken from 10 images. During the averaging process, white pixel values are not included. This image fusion method effectively reduces the influence of random points and enhances the visibility of features, particularly when the threshold is set to 7.

In the feature extraction stage, it is essential to extract the enhanced Canberra distance from the image. This feature involves calculating the Canberra distance, maximum singular value, and contrast of the image. In this paper, for the feature extraction method of SDP images, the Canberra distance measures the similarity between the original grayscale image and the enhanced image.

The Canberra distance is calculated between 10 sets of SDP images and enhanced images under the same working conditions. The mean of these 10 Canberra distances is taken as the feature. Table 2 presents the 10 repetitions of the Canberra distance calculated for each working condition. The table shows that the Canberra distance varies within a certain range under different working conditions. Specifically, the original Canberra distance of outer ring fault 2 is the smallest. Under normal status, the value of the original Canberra distance is the maximum. And it does not overlap with other working conditions. Based on Fig. 9 and Table 2, this result indicates that as the area of the pattern decreases, the Canberra distance of the image also decreases. The results also indicate that Canberra distance can achieve classification of fault types to a certain extent. However, the maximum value of ball fault 1 falls within the range of ball fault 2. This single feature fails to adequately classify the working conditions. Consequently, the original Canberra distance is enhanced by incorporating the maximum singular value and contrast.

According to Eq. 16, we first need to calculate the ratio between the maximum singular value and the Canberra distance. We use the singular value decomposition method to decompose the enhanced image. This process generates multiple singular values. The maximum singular value is an important feature of a data matrix. Therefore, among these multiple singular values, we select the maximum singular value as the feature of the enhanced image. Then, the ratio of the maximum singular value to the Canberra distance is calculated. At the same time, it is necessary to set a threshold k. When the threshold is set to 10, the ratio stays at a suitable size. Ten sets of each operating condition are randomly selected from the dataset, resulting in Table 3. In the table, we calculate the average maximum and minimum values of the 10 sets of features. From the table, we can discover that different working conditions have different ranges of features. This can provide reference standards for classification in the fault diagnosis stage.

The final stage of feature extraction involves calculating the contrast of the enhanced image. Contrast represents the texture and brightness characteristics of an image. For each working condition, calculate the contrast of the enhanced image using the principle of gray-level co-occurrence matrix and Eq. 13. Ten sets of contrast data were calculated for each operating condition, as shown in Table 4. From the results in the table, we can see that the contrast of normal status is the smallest, while the contrast of outer ring fault 2 is the highest. This result can be attributed to the smaller pattern of normal status, resulting in lower contrast. The pattern of outer ring fault 2 is larger and darker, resulting in higher contrast.

The integration of three features according to Eq. 11 yields an enhanced Canberra distance. Figure 11 illustrates a scatter diagram representing three features in a three-dimensional space. The x-axis corresponds to the Canberra distance. The y-axis corresponds to the maximum singular value. The z-axis represents the contrast of the image. Each working condition is visually represented by distinct colors in the three-dimensional space. In the xy plane, it is evident that the Canberra distance is inversely proportional to the maximum singular value. Hence, dividing the maximum singular value by the Canberra distance reduces the feature's order of magnitude and dimension. The figure indicates that the working conditions represented by different colors are

Table 2 The original Canberra distance between the original image and the enhanced image

Group	Normal status	Inner ring fault 1	Inner ring fault 2	Inner ring fault 3	Outer ring fault 1	Outer ring fault 2	Outer ring fault 3	Ball fault 1	Ball fault 2	Ball fault 3
1	75.16	46.61	40.36	30.62	65.89	22.39	35.03	57.55	61.98	51.50
2	76.00	44.96	41.54	28.88	64.35	23.63	35.79	57.68	59.71	52.65
3	75.84	43.56	41.45	31.71	63.29	23.90	35.09	58.51	60.51	52.87
4	73.47	46.02	39.94	33.36	64.38	22.72	35.47	58.81	61.86	53.32
5	77.66	47.27	39.19	28.74	65.10	22.53	35.47	57.83	58.74	50.34
6	73.64	44.26	40.29	31.55	65.89	24.31	35.38	58.38	61.94	50.58
7	75.58	45.34	40.46	31.43	65.20	24.62	35.46	59.33	62.63	52.82
8	74.83	45.29	39.43	31.06	64.78	22.80	34.14	57.96	61.13	51.73
9	75.60	42.99	40.60	28.42	63.40	24.43	35.51	57.32	58.91	50.13
10	70.94	46.79	40.95	29.06	65.20	22.22	34.57	56.38	59.80	47.33
Average	74.87	45.31	40.42	30.48	64.75	23.36	35.19	57.97	60.72	51.33
Maximum value	77.66	47.27	41.54	33.36	65.89	24.62	35.79	59.33	62.63	53.32
Minimum value	70.94	42.99	39.19	28.42	63.29	22.22	34.14	56.38	58.74	47.33

Table 3 The ratio of maximum singular value to Canberra distance for ten operating conditions

Group	Normal status	Inner ring fault 1	Inner ring fault 2	Inner ring fault 3	Outer ring fault 1	Outer ring fault 2	Outer ring fault 3	Ball fault 1	Ball fault 2	Ball fault 3
1	225.28	385.15	469.57	607.83	277.75	884.34	527.53	315.19	288.00	359.76
2	222.94	385.88	464.34	593.81	266.37	763.56	522.42	315.38	285.19	349.46
3	230.09	414.78	476.41	667.59	280.63	810.19	521.06	314.33	286.83	375.17
4	235.31	381.61	464.66	541.07	270.79	786.53	507.87	309.89	291.04	363.42
5	239.67	390.05	471.50	635.34	269.63	878.92	532.06	312.02	285.80	378.67
6	229.53	393.47	466.21	573.08	274.37	797.09	512.27	320.94	291.16	367.34
7	229.88	400.60	426.74	570.17	272.84	832.36	514.83	308.51	289.41	345.77
8	235.02	386.19	449.46	612.67	268.79	851.25	537.61	301.53	290.43	364.57
9	230.95	398.67	472.59	596.07	282.81	853.83	513.12	307.89	296.74	359.37
10	226.06	420.09	429.30	633.34	277.59	814.77	512.18	305.07	297.43	332.94
Average	230.47	395.65	459.08	603.10	274.16	827.28	520.10	311.08	290.20	359.65
Maximum value	239.67	420.09	476.41	667.59	282.81	884.34	537.61	320.94	297.43	378.67
Minimum value	222.94	381.61	426.74	541.07	266.37	763.56	507.87	301.53	285.19	332.94

Table 4 Contrast of enhanced images for 10 operating conditions

Group	Normal Status	Inner ring fault 1	Inner ring fault 2	Inner ring fault 3	Outer ring fault 1	Outer ring fault 2	Outer ring fault 3	Ball fault 1	Ball fault 2	Ball fault 3
1	0.365	0.614	0.640	0.771	0.520	0.717	0.638	0.640	0.581	0.674
2	0.363	0.613	0.626	0.770	0.496	0.700	0.633	0.627	0.576	0.664
3	0.386	0.630	0.631	0.779	0.521	0.694	0.631	0.626	0.584	0.684
4	0.410	0.615	0.635	0.744	0.500	0.685	0.627	0.608	0.589	0.642
5	0.416	0.615	0.633	0.779	0.498	0.703	0.628	0.621	0.577	0.646
6	0.379	0.619	0.638	0.757	0.503	0.690	0.627	0.637	0.589	0.647
7	0.382	0.625	0.606	0.759	0.498	0.696	0.626	0.613	0.584	0.652
8	0.408	0.619	0.624	0.776	0.502	0.692	0.633	0.595	0.582	0.673
9	0.376	0.619	0.634	0.772	0.525	0.695	0.627	0.607	0.596	0.649
10	0.375	0.630	0.604	0.765	0.515	0.704	0.637	0.602	0.601	0.649
Average	0.386	0.620	0.627	0.767	0.508	0.698	0.631	0.617	0.586	0.658
Maximum value	0.416	0.630	0.640	0.779	0.525	0.717	0.638	0.640	0.601	0.684
Minimum value	0.363	0.613	0.604	0.744	0.496	0.685	0.626	0.595	0.576	0.642

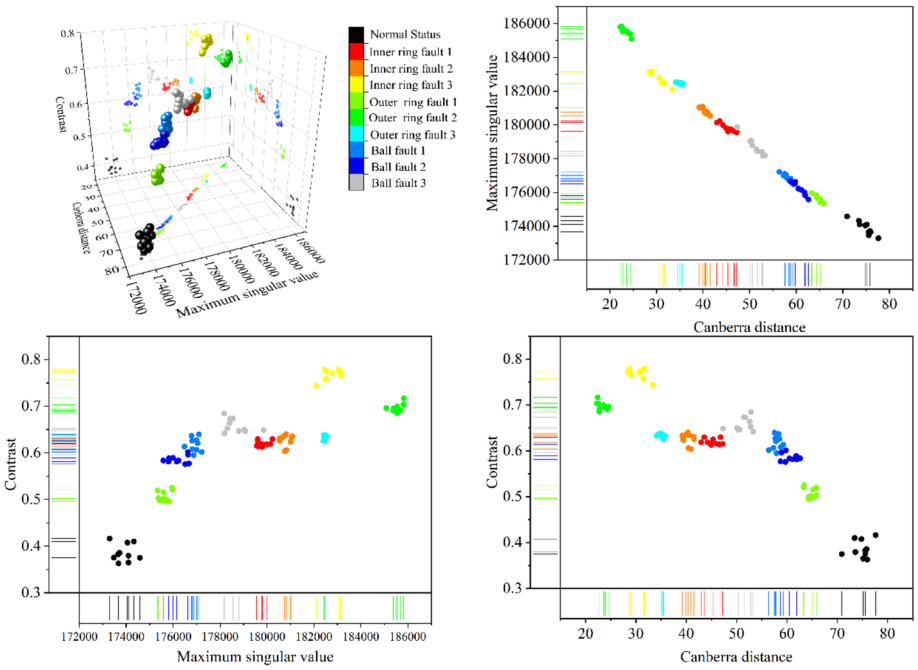

Fig. 11 The representation of Canberra distance, maximum singular value, and contrast in three-dimensional space

Table 5 Contrast of enhanced images for 10 operating conditions

Normal status	Ratio of maximum singular value to Canberra distance		Contrast	
	Lower bound	Upper bound	Lower bound	Upper bound
Normal status	222.94	239.67	0.36	0.416
Inner ring fault 1	381.61	420.09	0.61	0.630
Inner ring fault 2	426.74	476.41	0.60	0.640
Inner ring fault 3	541.07	667.59	0.74	0.779
Outer ring fault 1	266.37	282.81	0.50	0.525
Outer ring fault 2	763.56	884.34	0.69	0.717
Outer ring fault 3	507.87	537.61	0.63	0.638
Ball fault 1	301.53	320.94	0.60	0.640
Ball fault 2	285.19	297.43	0.58	0.601
Ball fault 3	332.94	378.67	0.64	0.684

concentrated in specific areas. Thus, the diagnosis of various working conditions can be achieved by demarcating specific areas for each condition.

During the fault diagnosis stage, upper and lower limits are established for the characteristics of each operating condition. The type of malfunction is determined based on whether the improved Canberra distance falls within the predefined range. In the feature extraction section, 10 sets of improved Canberra distances can be generated for each working condition. The maximum and minimum values of the ratio of the maximum singular value to the Canberra distance can be obtained from Table 3. Similarly, Table 4 provides the maximum and minimum values of contrast. These feature

ranges are organized in Table 5. The table represents the characteristic range of each fault type. Due to different images, the feature range of different fault types also varies. The image differences are converted into numerical differences for quantification. Therefore, by judging the characteristic values, the diagnosis of fault types can be achieved. These feature ranges will be used during the fault diagnosis phase. Firstly, it is necessary to perform image feature enhancement on signals of unknown fault types to enhance fault features. Then, the improved Canberra distance is obtained through feature extraction. Finally, the fault type is determined by comparing it with the feature range in Table 5.

To assess the efficacy of this method, we conducted a series of accuracy experiments. In the random experiments, we selected the latter half of the dataset. Additionally, we randomly selected fault types to validate the classification performance of our method in this paper. When a feature falls within the range of Table 6, we check whether the diagnosed fault type matches the actual type. The number of accurate judgments and the total number of judgments are recorded to calculate the overall test accuracy. Table 6 presents the accuracy rates from 10 tests conducted after image enhancement, each consisting of 500 judgments. The highest accuracy rate among the 10 test groups is 99.60%, with an average accuracy rate exceeding 99%. The experimental results show that this method can classify various fault types effectively.

Comparative experiment 1: With original Canberra distance

In order to verify the effectiveness of feature diagnosis, the original Canberra distance is compared with the improved accuracy. The original Canberra distance only uses one indicator of the original Canberra distance to test the accuracy. Run 10 times to obtain the accuracy of each time as shown in Table 7. The average accuracy of the original Canberra distance is 92.02%, the maximum accuracy is 92.79%, and the minimum accuracy is 91.18%. The average accuracy is 7.04% lower than that in this paper. However, only Canberra distance is used in the enhanced image, which also achieves more than 90% accuracy.

Table 6 Accuracy after image enhancement

Group	Accuracy
1	99.00%
2	99.20%
3	99.60%
4	98.39%
5	99.60%
6	98.80%
7	98.39%
8	99.20%
9	98.80%
10	99.60%
Average	99.06%
Maximum value	99.60%
Minimum value	98.39%

Table 7 Accuracy after image enhancement

Group	Original Canberra distance	Present method
1.00	92.79%	99.00%
2.00	92.38%	99.20%
3.00	92.18%	99.60%
4.00	91.58%	98.39%
5.00	92.38%	99.60%
6.00	91.18%	98.80%
7.00	92.38%	98.39%
8.00	91.18%	99.20%
9.00	91.58%	98.80%
10.00	92.59%	99.60%
Average	92.02%	99.06%
Maximum value	92.79%	99.60%
Minimum value	91.18%	98.39%

Table 8 Comparison with non-enhanced images

Group	Non-enhancement condition	Present method
1	83.94%	99.00%
2	81.12%	99.20%
3	86.35%	99.60%
4	87.15%	98.39%
5	82.57%	99.60%
6	86.77%	98.80%
7	82.57%	98.39%
8	86.77%	99.20%
9	85.17%	98.80%
10	82.57%	99.60%
Average	84.50%	99.06%
Maximum value	87.15%	99.60%
Minimum value	81.12%	98.39%

The results in Table 7 indicate that the original Canberra distance has a certain degree of classification performance. The accuracy can be improved by using the maximum singular value and contrast. Compared to the original Canberra distance, there is an improvement in accuracy.

Comparative experiment 2: With non-enhancement condition

In order to verify the effectiveness of image enhancement, the effect without image enhancement is tested here. The difference before and after enhancement is whether 10 images are fused into 1 image. There is no image enhancement method to directly convert the signal into an image. The accuracy obtained from the test is shown in Table 8. The average accuracy of the enhanced method is 84.50%. Compared with the method after image enhancement, the average accuracy difference is 14.56%. The effect of enhancement is obvious. This shows that the fault feature of the image is indeed enhanced.

The results in Table 8 show that this method can highlight the features of the image. The proposed method enhances the accuracy of testing. The effect of the diagnosis is poor under the condition of no enhancement. This indicates that the fault features are not prominently visible in the image. By using the method of image feature enhancement, fault features can be detected more easily.

Comparative experiment 3: Under different noise conditions

In order to verify the effect of this method in noise environment, white noise with different signal-to-noise ratios is added to the original signal to test the accuracy. The accuracy of this method under different signal-to-noise ratios is shown in Table 9. With the increase of signal-to-noise ratio, the accuracy of the experiment also improves. From the table, we can see that the accuracy is 31.92% when the signal-to-noise ratio is 10 dB. When the signal-to-noise ratio is 20 dB, the accuracy is 79.70%. The signal-to-noise ratio has a significant impact on accuracy at 10 dB and 20 dB. When the signal-to-noise ratio is greater than 30 dB, the accuracy remains above 90%. In addition, with the increase of signal-to-noise ratio, the detection accuracy shows an upward trend. At a signal-to-noise ratio of 100 dB, the average detection accuracy is 94.74%.

Through the table, we can obtain the following results: the accuracy of the method is significantly affected by the signal-to-noise ratio at 10 dB. However, the method shows higher diagnostic efficiency under noise conditions above 20 dB. The reason behind this result is that the white noise below 20-dB masks the characteristics of most signals, resulting in the improvement of Canberra distance being unable to effectively achieve fault classification. Therefore, there are limitations to this method in a noise environment below 20 dB.

Comparative experiment 4: With different image enhancement methods

In order to thoroughly evaluate the influence of pixel value variations on enhanced image feature extraction, we utilized the maximum and minimum pixel values as control groups for extracting fault features. The fusion method for the maximum pixel

Table 9 Accuracy under different signal-to-noise ratios

Group	10 db	20 db	30 db	40 db	50 db	60 db	70 db	80 db	90 db	100 db
1	32.26%	80.36%	89.78%	94.39%	93.39%	95.18%	95.99%	94.59%	96.79%	94.38%
2	32.87%	81.16%	90.98%	94.19%	91.57%	93.57%	93.98%	93.57%	93.79%	95.18%
3	35.07%	77.35%	89.96%	93.17%	93.98%	94.38%	93.57%	94.38%	93.57%	94.78%
4.00	33.47%	80.76%	89.56%	90.76%	91.57%	93.57%	93.98%	94.38%	93.98%	94.38%
5.00	29.46%	81.16%	93.57%	93.98%	93.98%	94.38%	93.57%	93.17%	93.98%	93.57%
6.00	32.67%	79.56%	90.76%	93.17%	91.57%	93.57%	95.18%	94.38%	93.98%	95.98%
7.00	32.46%	77.96%	90.98%	90.76%	93.98%	94.38%	94.78%	95.18%	93.98%	93.17%
8.00	33.87%	77.56%	89.96%	91.57%	95.58%	94.78%	95.18%	95.58%	93.98%	94.78%
9.00	26.45%	80.56%	89.56%	90.98%	94.78%	94.38%	94.38%	95.58%	94.78%	95.18%
10.00	30.66%	80.56%	93.57%	90.76%	94.78%	95.18%	93.17%	93.17%	97.59%	95.98%
Average	31.92%	79.70%	90.80%	92.37%	93.52%	94.34%	94.38%	94.40%	94.64%	94.74%

value is represented by Eq. 19. On the other hand, the fusion method for the minimum pixel value is represented by Eq. 20. Compared to the original method, Eq. 19 selects the maximum pixel value from 10 images for the enhanced image pixel values. On the other hand, Eq. 20 selects the minimum pixel value from 10 images for the enhanced image's pixel values.

$$G_{max}(x,y) = \begin{cases} \underset{i=1,2,\ldots px}{max} \; (I_i(x,y)) & N_{px} < T \\ 255 & N_{px} \geq T \end{cases} \tag{19}$$

$$G_{min}(x,y) = \begin{cases} \underset{i=1,2,\ldots px}{min} \; (I_i(x,y)) & N_{px} < T \\ 255 & N_{px} \geq T \end{cases} \tag{20}$$

The control group utilized the maximum and minimum grayscale values from 10 images as the respective grayscale values for the enhanced images. The improved Canberra distance extracted through the maximum fusion method is shown in Fig. 12a. The improved Canberra distance obtained through the minimum value fusion method is displayed in Fig. 12b. Figure 12c exhibits the improved Canberra distance acquired via the enhanced weighted average method. The horizontal axis represents the number of calculation groups, with 10 sets calculated for each method. The vertical axis signifies the enhanced Canberra distance. In the blue box of Fig. 12a, the features of outer ring fault 1 and ball fault 2 intersect. This indicates that the method cannot accurately classify these two types of faults. The same phenomenon is also observed in Fig. 12b. When features become entangled, it becomes challenging to accurately distinguish the two working conditions. This article effectively addresses this phenomenon in the employed improved weighted average method. It effectively disentangles the entanglement between the two working conditions.

Comparative experiment 5: With different datasets

The comparative experiment is conducted using data obtained from Southeast University (https://www.github.com\\/cathysiyu/Mechanical-datasets). The working conditions consist of normal status, inner ring fault, outer ring fault, and ball fault. The dataset is obtained from the Drivetrain Dynamics Simulator. We selected the motor vibration

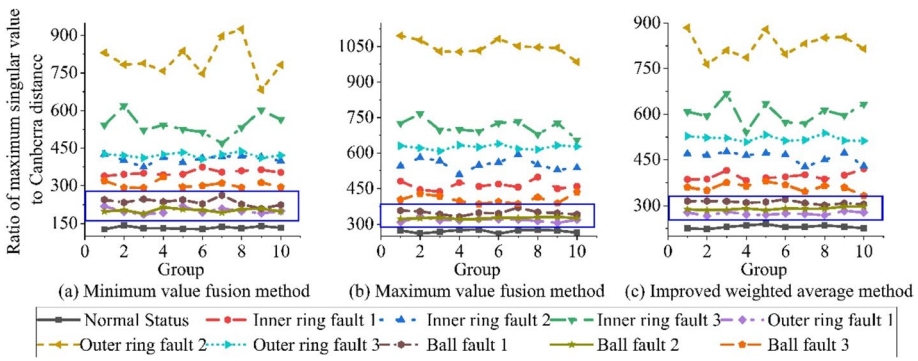

Fig. 12 Improved Canberra distance features for different enhancement methods

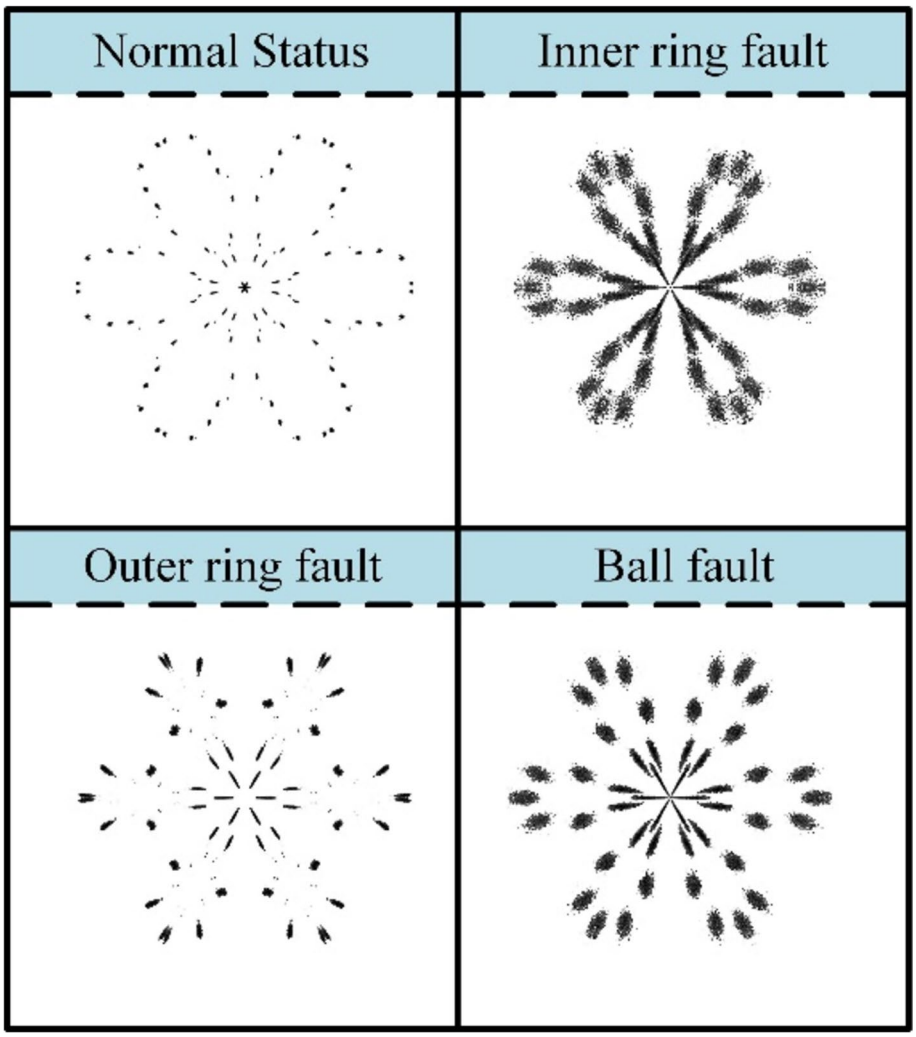

Fig. 13 SDP images from the bearing dataset of Central South University

signals from the dataset. The motor vibration signals for the four fault types are plotted as SDP images, as shown in Fig. 13.

The differences between the SDP images for each working condition are visually apparent. The SDP image for the normal status exhibits a distinct outline. The SDP image for the inner ring fault shows a more pronounced contrast. The SDP images for the outer ring fault display a block-based distribution. Ball faults also show a block distribution. However, compared to the SDP image of the outer ring fault, the image contour of the ball fault is more distinct.

To validate the effectiveness of the proposed classification method, various feature classification methods were incorporated in this experiment. Simultaneously, we introduce varying levels of white noise to the signal in order to conduct accuracy experiments. This is done to demonstrate the noise resistance ability of the proposed method in this paper. The experimental results are illustrated in Fig. 14.

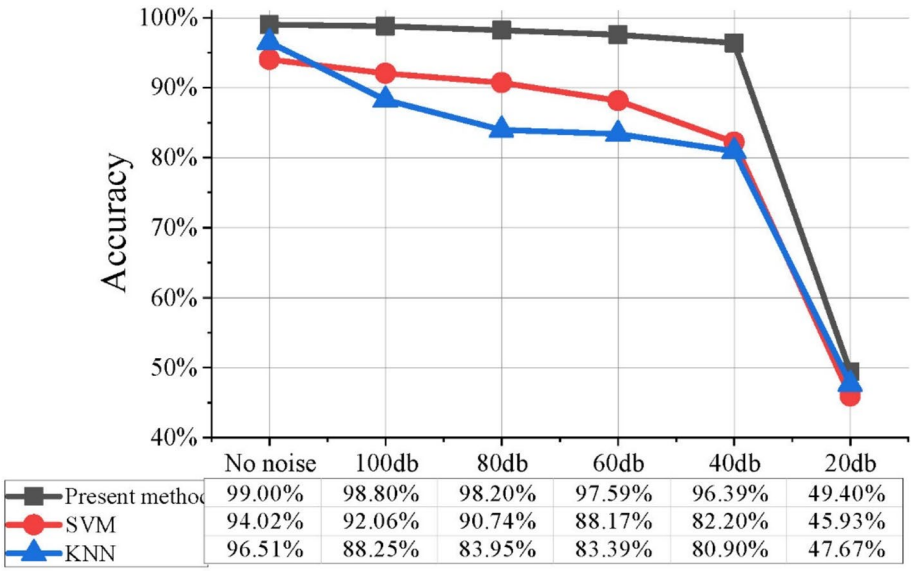

Fig. 14 Classification accuracy under different methods and signal-to-noise ratios

The images demonstrate that the current method in this dataset consistently achieves high classification performance. It also maintains high classification accuracy in noisy environments. The current method maintains an accuracy of over 96% even when the signal-to-noise ratio exceeds 40 dB. Moreover, the proposed method surpasses the performance of both the support vector machine (SVM) and K-nearest neighbors (KNN) methods in terms of classification.

Limitations and implications of research findings in the current research context

The research content of this article has significant implications in the current research context. Currently, many fields have applied SDP signal processing methods. The content of this article can be to enhance image features, which is very meaningful for fault diagnosis using signals. The extraction of fault features from SDP images is a simple and effective method. An advantage of SDP images is their independence from mechanical power or configuration. Furthermore, they are applicable to various signal types. However, this conversion method does have limitations. Firstly, the image features may not fully capture the signal changes. Additionally, features can be lost during the process of data-to-image conversion. The conversion of data into images serves as a means to increase data dimensionality. The image format complicates the calculation process. This presents challenges for image processing and feature extraction. Achieving signal feature representation with reduced computational time and feature count is a potential challenge. Another potential research avenue involves employing image features to predict mechanical lifespan.

Conclusions

In this paper, a method of image enhancement based on image fusion is proposed. This method is applied to the fault diagnosis of mechanical vibration signals, and the enhancement of the synchronized dot pattern image features of vibration signal conversion is realized. In addition, the improved Canberra distance is used to extract image fault features. In this paper, vibration signal processing, feature extraction and fault classification are realized. At the same time, different experiments are carried out using the data of rolling bearings. In the comparison of original images, the effectiveness of the image enhancement method in this paper is verified. In the comparison test with the original Canberra distance, the effectiveness of the improved Canberra distance using the maximum singular value and contrast is verified. Finally, the robustness of the image enhancement method and feature extraction ability under the influence of different intensities of noise is analyzed. Therefore, the image enhancement method proposed in this paper has high reliability and classification accuracy in fault diagnosis using the synchronized dot pattern.

Abbreviations

STFT	Short-time Fourier transform
SDP	Symmetrized dot pattern
VMD	Variational mode decomposition
SVM	Support vector machine
KNN	K-nearest neighbors
IMF	Intrinsic mode function

Acknowledgements
This work is supported by National Natural Science Foundation of China (No. 61603149) and Shandong Province Natural Science Foundation (No. ZR2023MF102).

Authors' contributions
JGP is responsible for writing and rewriting the article, revising the article, simulating the program. YJS is responsible for providing ideas and formulating research directions. WW is responsible for building the framework and writing of the first draft. All authors have read and approved the manuscript.

Funding
This work is supported by National Natural Science Foundation of China (No. 61603149) and Shandong Province Natural Science Foundation (No. ZR2023MF102).

Availability of data and materials
It will be made available on request.

Declarations

Competing interests
The authors declare that they have no competing interests.

Received: 21 July 2023 Accepted: 30 September 2024
Published online: 08 October 2024

References

1. Liu ZH, Lu BL, Wei HL et al (2020) A stacked auto-encoder based partial adversarial domain adaptation model for intelligent fault diagnosis of rotating machines. IEEE Trans Industr Inf 17(10):6798–6809
2. Zhang L, Zhang F, Qin Z et al (2022) Piezoelectric energy harvester for rolling bearings with capability of self-powered condition monitoring. Energy 238:121770
3. Zhang Y, Cao J, Zhu H et al (2019) Design, modeling and experimental verification of circular Halbach electromagnetic energy harvesting from bearing motion. Energy Convers Manage 180:811–821
4. He M, He D (2020) A new hybrid deep signal processing approach for bearing fault diagnosis using vibration signals. Neurocomputing 396:542–555
5. Wang T, Qiao M, Zhang M et al (2020) Data-driven prognostic method based on self-supervised learning approaches for fault detection. J Intell Manuf 31:1611–1619

6. Altan A, Karasu S, Bekiros S (2019) Digital currency forecasting with chaotic meta-heuristic bio-inspired signal processing techniques. Chaos Solitons Fractals 126:325–336
7. Altan A, Karasu S, Zio E (2021) A new hybrid model for wind speed forecasting combining long short-term memory neural network, decomposition methods and grey wolf optimizer. Appl Soft Comput 100:106996
8. Wu P, Lou S, Zhang X et al (2020) Data-driven fault diagnosis using deep canonical variate analysis and fisher discriminant analysis. IEEE Trans Industr Inf 17(5):3324–3334
9. Li C, Li S, Zhang A et al (2021) Meta-learning for few-shot bearing fault diagnosis under complex working conditions. Neurocomputing 439:197–211
10. Liu C, Zhang L, Niu J et al (2020) Intelligent prognostics of machining tools based on adaptive variational mode decomposition and deep learning method with attention mechanism. Neurocomputing 417:239–254
11. Özçelik YB, Altan A (2023) Overcoming nonlinear dynamics in diabetic retinopathy classification: a robust AI-based model with chaotic swarm intelligence optimization and recurrent long short-term memory. Fractal and Fractional 7(8):598
12. Bai Y, Yang J, Wang J et al (2021) Image representation of vibration signals and its application in intelligent compound fault diagnosis in railway vehicle wheelset-axlebox assemblies. Mech Syst Signal Process 152:107421
13. Chang L, Liu Z, Shen Y et al (2020) Novel multistate fault diagnosis and location method for key components of high-speed trains. IEEE Trans Industr Electron 68(4):3537–3547
14. Kim Y, Na K, Youn BD (2022) A health-adaptive time-scale representation (HTSR) embedded convolutional neural network for gearbox fault diagnostics. Mech Syst Signal Process 167:108575
15. Wu J, Tang T, Chen M et al (2020) A study on adaptation lightweight architecture based deep learning models for bearing fault diagnosis under varying working conditions. Expert Syst Appl 160:113710
16. Jablonski A, Dziedziech K (2022) Intelligent spectrogram-a tool for analysis of complex non-stationary signals. Mech Syst Signal Process 167:108554
17. Wodecki J, Kruczek P, Bartkowiak A et al (2019) Novel method of informative frequency band selection for vibration signal using nonnegative matrix factorization of spectrogram matrix. Mech Syst Signal Process 130:585–596
18. Reinhold I, Sandsten M (2022) The multitaper reassigned spectrogram for oscillating transients with Gaussian envelopes. Signal Process 198:108570
19. Peng C, Zou J, Liang M et al (2020) A novel linear CCD variable velocity two-dimensional imaging approach based on adaptive image segmentation. IEEE/ASME Trans Mechatron 25(2):762–769
20. Long Z, Zhang X, He M et al (2021) Motor fault diagnosis based on scale invariant image features. IEEE Trans Industr Inf 18(3):1605–1617
21. Wang XB, Luo L, Tang L et al (2021) Automatic representation and detection of fault bearings in in-wheel motors under variable load conditions. Adv Eng Inform 49:101321
22. Tang H, Liao Z, Chen P et al (2020) A novel convolutional neural network for low-speed structural fault diagnosis under different operating condition and its understanding via visualization. IEEE Trans Instrum Meas 70:1–11
23. Li C, Mo L, Yan R (2021) Fault diagnosis of rolling bearing based on WHVG and GCN. IEEE Trans Instrum Meas 70:1–11
24. Fang H, Deng J, Zhao B et al (2021) LEFE-Net: a lightweight efficient feature extraction network with strong robustness for bearing fault diagnosis. IEEE Trans Instrum Meas 70:1–11
25. Wang T, Liu Z, Lu G et al (2020) Temporal-spatio graph based spectrum analysis for bearing fault detection and diagnosis. IEEE Trans Industr Electron 68(3):2598–2607
26. Nath AG, Udmale SS, Raghuwanshi D et al (2021) Improved structural rotor fault diagnosis using multi-sensor fuzzy recurrence plots and classifier fusion. IEEE Sens J 21(19):21705–21717
27. Sun Y, Li S, Wang X (2021) Bearing fault diagnosis based on EMD and improved Chebyshev distance in SDP image. Measurement 176:109100
28. Wang H, Wu F, Zhang L (2021) Application of variational mode decomposition optimized with improved whale optimization algorithm in bearing failure diagnosis. Alex Eng J 60(5):4689–4699
29. Chen P, Zhao X, Zhu Q (2020) A novel classification method based on ICGOA-KELM for fault diagnosis of rolling bearing. Appl Intell 50:2833–2847
30. Sun Y, Li S, Wang Y et al (2021) Fault diagnosis of rolling bearing based on empirical mode decomposition and improved Manhattan distance in symmetrized dot pattern image. Mech Syst Signal Process 159:107817